PCCP

PAPER

View Article Online
View Journal | View Issue

Cite this: *Phys. Chem. Chem. Phys.*, 2015, **17**, 29311

Inclusion of supported gold nanoparticles into their semiconductor support†

Marcus Lau, Anna Ziefuss, Tim Komossa and Stephan Barcikowski*

Received 22nd July 2015,
Accepted 1st October 2015

DOI: 10.1039/c5cp04296h

www.rsc.org/pccp

Supported particles are easily accessible as standard materials used in heterogeneous catalysis and photocatalysis. This article addresses our exemplary studies on the integration of supported nanoparticles into their solid support, namely gold nanoparticles into zinc oxide sub-micrometer spheres, by energy controlled pulsed laser melting in a free liquid jet. This one-step, continuous flow-through processing route reverses the educt's structure, converting the ligand-free surface adsorbate into a spherical subsurface solid inclusion within its former support. The results show how a nanoparticulate surface adsorbate can be included in the form of crystalline nanoparticles into the resolidified support matrix, demonstrated by using plasmonic nanoparticles and semiconductor microparticles as reference materials.

Introduction

Supported metal nanoparticles on metal oxides are commonly available raw materials with application prospects in catalysis.[1–3] For example, gold nanoparticles (Au NPs) on a zinc oxide (ZnO) support can catalyze chemical reactions.[4] Even though gold nanoparticles can be easily attached to ZnO nanoparticles[5,6] their integration into a zinc oxide matrix on the nanoscale is challenging. A possibility to melt aqueous dispersions of particulate materials under non-equilibrium conditions is pulsed laser melting in liquid (PLML). PLML has been shown to be an effective synthesis route for crystalline sub-micrometer spheres (SMS), but additive PLML has only rarely been investigated and this has not covered supported particles yet.

The fabrication of SMS by PLML is a technique pioneered by Koshizaki and coworkers.[7,8] Early application examples have been demonstrated by Hu *et al.* for SMS in lubricant oils to reduce the friction coefficient,[9] and Fujiwara *et al.* who used ZnO SMS as a light emitting laser source.[10]

Since the first report several articles report the possibility and power of this technique. In contrast to size-reducing pulsed laser fragmentation in liquid (PLFL), lower laser fluences are required, resulting in particle melting and resolidification as spheres. Wang *et al.* found the onset laser fluence for particle melting of zinc oxide to be between 33 mJ cm^{-2} and 67 mJ cm^{-2}.[8] A limitation to high laser fluences was reported by Wang *et al.* for the laser melting of CuO nanoparticles to copper SMS.[11] At a fluence of 150 mJ cm^{-2} the SMS showed a rough surface. This indicates less effective particle melting due to onset of particle fragmentation. The influence of educt particle size on melting effectivity was demonstrated by Tsuji *et al.*[12] They showed that by increasing the educt particle size of ZnO particles the fluence required for sufficient PLML to obtain monomodal and smooth ZnO SMS increases. Namely 70 nm ZnO educt particles were molten completely at fluences of 100 mJ cm^{-2} whereas aggregated (500 nm aggregate diameter) ZnO educt particles were only partially molten at laser fluences of 200 mJ cm^{-2} and completely molten at fluences of 300 mJ cm^{-2}.[12] Liu *et al.* demonstrated that PLML appears to be an isochoric process using octahedral Au NPs, and transformed them into monodisperse Au nanospheres preserving the volume of the particles, thus demonstrating that PLML can be applied as an isochoric particle reshaping method.[13]

First reports on the laser melting of Au NPs were given by El-Sayed and coworkers[14–16] who reported the sufficient interaction of surface plasmons with 532 nm laser light for the isochoric melting of Au nanorods to nanospheres. In 2005 Inasawa *et al.* showed that for gold nanoparticles the melting temperature is approximately 100 K below the value of the bulk material, using nanoparticles around 38 nm and applying a laser wavelength of 355 nm.[17] Tsuji and coworkers recently reported the possibilities to melt aggregated Au NPs to SMS with 532 nm laser light and found a PLML induction time interval caused by the laser-induced surfactant removal.[18,19]

Studies on SMS formation mostly report the use of 355 nm laser wavelength and nanosecond pulses to cause distinctive particle melting in liquid, even though other wavelengths and shorter (ps) pulse lengths are able to cause (partial) melting as well.[20]

Besides simple physical melting, changes in chemical composition are also reported.[7,11,21] Ishikawa *et al.* studied the formation of

Technical Chemistry I, University of Duisburg-Essen and Center for Nanointegration Duisburg-Essen (CENIDE), Universitaetsstr. 7, 45141 Essen, Germany.
E-mail: stephan.barcikowski@uni-due.de

† Electronic supplementary information (ESI) available: Further characterization of the material before and after laser melting. The characterization includes the determination of particle load on the support from different approaches, optical characterization, particle size distributions and additional SEM images. See DOI: 10.1039/c5cp04296h

boron carbide SMS from boron nanoparticles in organic solvents. Additionally, PLML-alloying of non-equilibrium phases is known.[22] Swiatkowska-Warkocka *et al.* generated bimetallic crystalline SMS of copper and gold, but they obtained a solid solution in contrast to the inclusion type of SMS reported here. Nakamura *et al.* recently reported on magnetite particles integrated into calcium phosphate SMS by the combination of chemical precipitation and a laser wavelength absorbance of the iron salt, which was subsequently integrated into the calcium salt SMS during PLML.[23] Hence, the investigation on the integration of iron into SMS included chemical reactions and complex precipitation-reaction-melting inter-dependence.[23] Next to reactive PLML or the alloying of miscible elements, the question arises as to what happens during the irradiation of partly miscible or immiscible mixtures under PLML conditions. PLML of a colloidal mixture of gold with as-prepared iron oxide nanoparticles resulted in a core–shell structure with a porous surface after Fe etching,[24–26] but supported particles have not yet been investigated.

In this context the facile synthesis of supported particles comes into play, such as the adsorption of ligand-free metal nanoparticles (Au, Ag, Pt, Pd) on supports (ZnO, TiO_2, $BaSO_4$, graphene)[27] simply by mixing at defined liquid parameters,[28] thus achieving up to a 60 wt% NP-on-support at 100% yield. Taking Au/ZnO as a relevant example (*e.g.* for photocatalysis applications), it was uncertain what will happen if this nano/micro support system is exposed to PLML and motivating the present study.

Experimental

The preparation of supported particles followed the mechanism firstly reported by Wagener *et al.*[27] and described in detail by Marzun *et al.*,[28] where the Au/ZnO preparation procedure was analogous to that of Lau *et al.*[6] Au NPs were generated by picosecond pulsed laser ablation in liquids (PLAL) in 600 μM of aqueous phosphate buffer to create small particles, and size separation was conducted by centrifugation using an Ultracentrifuge (Beckman Coulter), with a force of 30 000*g* for 14 minutes resulting in a monodisperse Au NP colloid with a defined concentration. Concentration of the supernatant was determined from the extinction at a fixed wavelength subsequent to calibration with different concentrations of the same particle size. The monodisperse Au colloid had a concentration of 62.7 ± 0.1 μg mL^{-1} after centrifugation. We added 95 mg zinc oxide particles to an overall colloid volume of 450 mL Au NPs in water resulting in an Au NP loading of 30 wt% adsorbed on to zinc oxide after 100% Au NP adsorption. Detailed particle size distributions (mass-weighted 5 ± 0.9 nm, number-weighted 4.7 ± 0.8 nm) and the determination of concentration using calibrated UV-vis spectroscopy of the monodisperse Au NP colloids (polydispersity index < 0.03) are provided in Fig. S1 of ESI.† Zinc oxide particles (Sigma Aldrich) were simply added to the monodisperse gold nanoparticle suspensions and the obtained gold/zinc oxide supported particle powder was dried (50 °C, 8 h). Note that there are different values describing the amount of supported nanoparticles. Fig. S2 (ESI†) illustrates the absolute wt% of nanoparticles plotted *versus* the wt% of gold nanoparticles adsorbed onto zinc oxide as a support, resulting in a nonlinear correlation between the wt% and vol%. The volume percentage might be of interest as the optical response and colloidal analytics often correlate to the particle volume, but in catalysis applications wt% is the standard unit. For PLML the highest amount of supported gold nanoparticles used in this study was 30 wt% of gold adsorbed on the support (thus a gold amount of approx. 23 wt% absolute), equivalent to 11 vol% (see Fig. S2, ESI†).

Laser irradiation was performed with an Nd:YAG laser operating at the 3rd harmonic (355 nm wavelength) with 85 kHz repetition rate, 23 watt and a pulse length of 40 ns.

For the determination of the influence of laser fluence on PLML and the defined volume-specific laser energy dose we used the design of a sequential liquid flow. This design has been reported previously and allows the study of the impact of the applied laser fluence while focusing on a thin liquid filament.[20] Hence, the minimized beam path in liquid significantly reduces fluence variation along beam propagation, allowing defined energy balancing. As reported before, a strong shift of a local peak in the UV/vis spectrum can be attributed to a sufficient PLML effect.[20] Thus, plotting the observed shift of this local peak can be used to draw conclusions for the PLML efficiency and the applied laser fluence. To study the influence of the applied laser fluence pure zinc oxide particles were used.

The PLML of the supported Au/ZnO was conducted under the optimized conditions found for pure zinc oxide in pure water with no additives. All the suspensions used for laser irradiation had a particle concentration of 0.1 wt% as this was found to be appropriate to characterize PLFL and PLML sufficiently.[20]

Size characterization of the particles was performed with an analytical disc centrifuge (CPS instruments) at 24 000 rpm, and extinction of the colloids was determined with an UV-vis absorbance spectrometer (evolution 201) in a quartz glass cuvette. Diffuse powder reflection was determined in a spectrometer (Varian Cary) using a Spectralon reference (PTFE). SEM images were taken with an SEM (FEI Quanta 400) on carbon supports. XRD measurements of the compound particles before and after PLML were carried out with a Cu Kα irradiation source at 40 kV and 40 mA in a Bruker D8 Advance system.

The preparation route for the nano/micro support systems used here is schematically shown in Fig. 1.

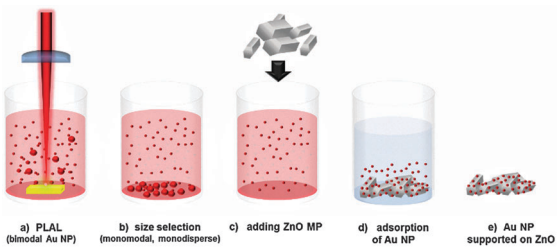

Fig. 1 Schematic illustration of the process steps to fabricate supported Au NP/ZnO MPs with monodisperse nanoparticles attached to the support: (a) picosecond-pulsed laser ablation in water (PLAL); (b) size selection by centrifugation; (c) addition of zinc oxide microparticles to the gold colloid; (d) adsorption of gold nanoparticles onto the zinc oxide microparticles; (e) dried powder for further PLML processing.

Results and discussion

We demonstrate how plasmonic nanoparticles can be embedded into semiconductor sub-micrometer spheres by laser melting in a continuous liquid flow. This route allows the achievement of an integration of metallic nanoparticles into a semiconductor SMS matrix in one step without performing any chemical precursor-based synthesis. Within our experiments only pure water was used as a carrier liquid. A fluid jet reactor setup was applied allowing precise fluence control and sequential analysis of the product evolution after defined PLML passage numbers. As shown in Fig. 2(a) the variation of the laser fluence results in significant shifts of the local UV-vis peak positions. Variation of the laser fluence to determine the fluence regime for zinc oxide particle melting was performed with pure zinc oxide particles. Corresponding UV-vis spectra for pure zinc oxide from which the peak shift is determined, are shown in Fig. S3 in the ESI.† The bathochromic shift of the peak can be correlated to the ZnO particle melting and resolidification as spheres. Thus plotting this shift *versus* the laser fluence illustrates the process window for PLML (at 355 nm laser wavelength and 40 ns pulse length), indicated in Fig. 2(a) to be ≤ 0.2 J cm^{-2}. Fig. 2(b) shows the powder scattering spectra for pure zinc oxide and for the supported Au NP on the ZnO MP with a 30 wt% gold loading. The diffuse reflection spectra show that the increased extinction at wavelengths above 600 nm results from light scattering.[29] This diffuse reflection is caused by spheres formed by PLML, as proposed by Wang *et al.*[8] That such spheres reflect light wavelengths in their size regime is confirmed here by the scattering measurement of the dried particle powders. Additionally, the relative minimum absorption of Au NPs in the scattering spectra around 550 nm can be observed from the diffuse reflection which becomes more distinctive after 50 passages of PLML due to the size increase of the Au NPs. UV-vis spectra before and after 50 passages of laser melting in liquid filament are shown in Fig. 2(c) and (d) with SEM images of the corresponding educt and product particles as insets. For the semiconductor SMS products with gold nanoparticle inclusion, two peaks in the visible regime are obtained. For the educt gold nanoparticle size a plasmon peak around 550 nm is observed. In the course of laser melting and reversing the particle structure from supported Au NP to solid Au NP inclusions, obviously the Au NP size increases as validated by the SEM pictures (Fig. S5, ESI†).

UV-vis spectra in Fig. 3 show the difference between the PLML of pure ZnO and the PLML of 30 wt% Au NPs with ZnO. The evolution of the local peak around 600 nm can be attributed to the scattering of light on the formed spheres with sizes in this wavelength regime. This scattering effect occurs for pure ZnO

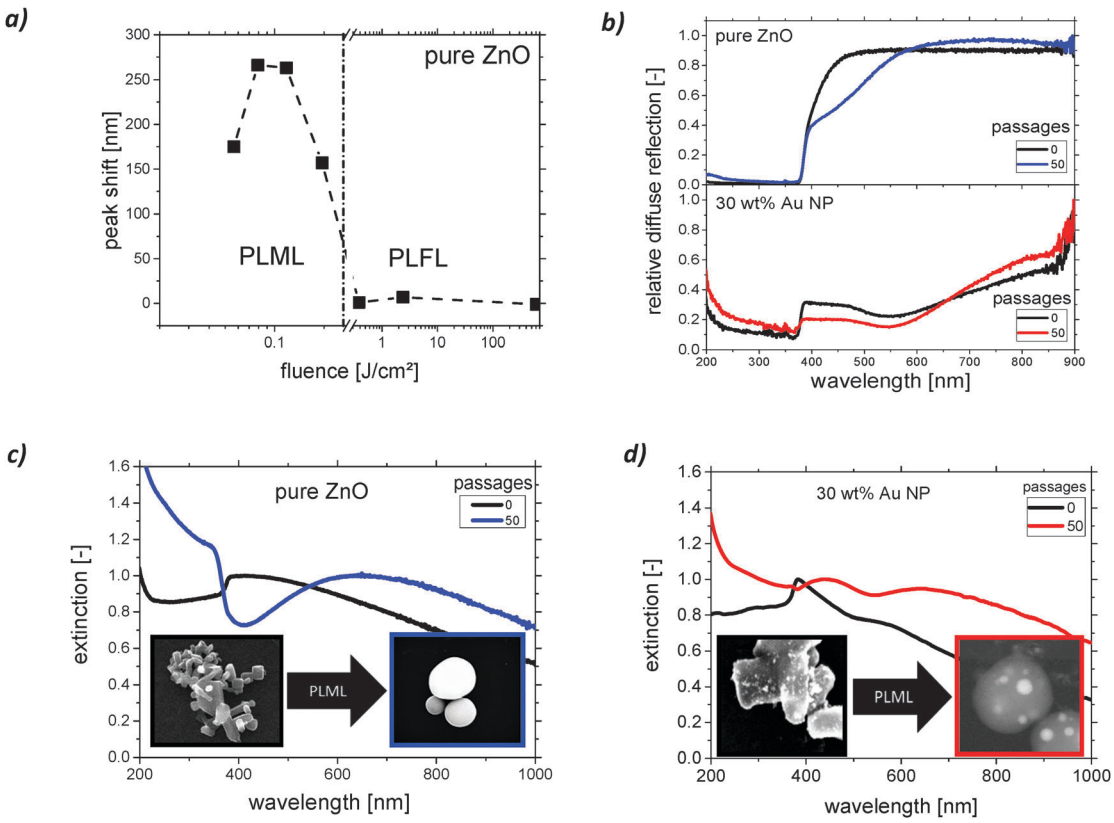

Fig. 2 (a) Impact of the laser fluence on the UV-vis peak shift of the zinc oxide suspension after laser irradiation (at 355 nm and 40 ns); (b) relative diffuse scattering of the dried particle powders before and after 50 passages of PLML for pure ZnO (top) and 30 wt% Au NP supported on ZnO (bottom); (c) normalized (at peak in visible regime) UV-vis spectrum of pure zinc oxide particles before (black line) and after (blue line) PLML in pure water with SEM images of corresponding educt and product particles as inset; (d) normalized UV-vis spectrum of zinc oxide particles with 30 wt% supported gold nanoparticles before (black line) and after (red line) PLML in pure water.

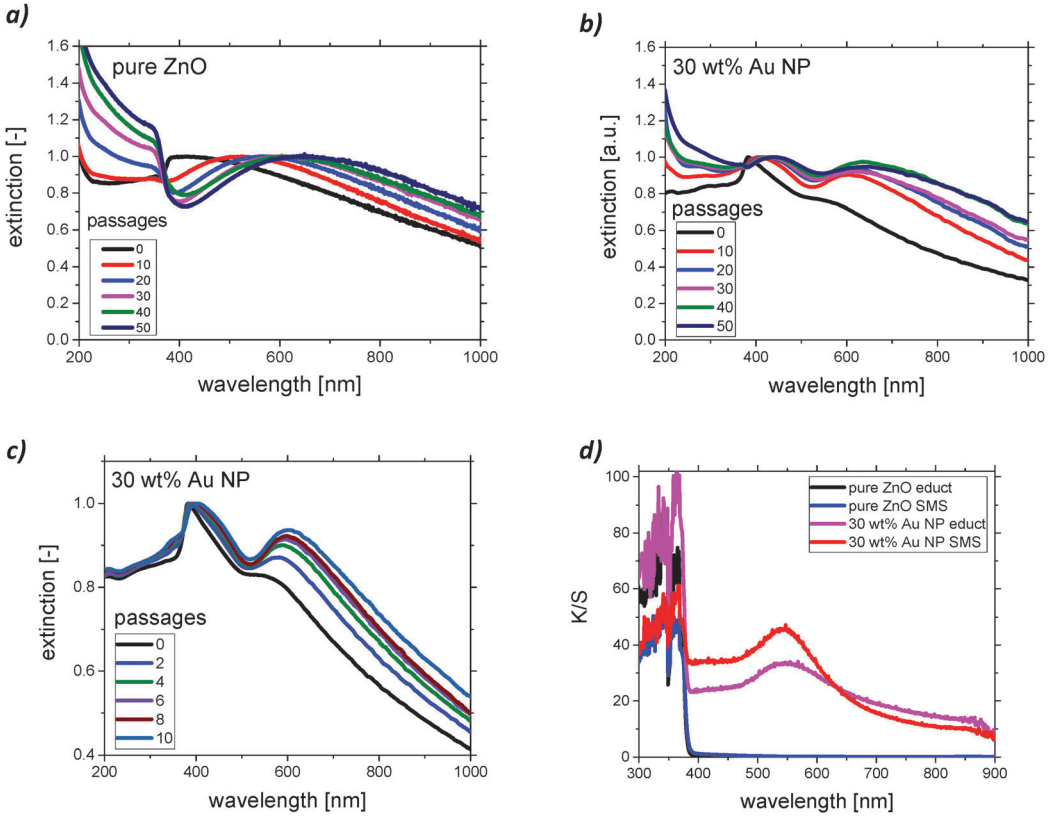

Fig. 3 The evolution of UV-vis spectra during PLML with a fluence of 80 mJ cm^{-2} normalized at a peak in the visible regime for (a) pure zinc oxide after each 10 passages from 0 to 50 irradiation cycles, for (b) 30 wt% Au NPs on ZnO after each 10 passages from 0 to 50 irradiation cycles and (c) for 30 wt% Au NPs on ZnO after every second cycle during first 10 passages; (d) the ratio of absorption to scattering K/S determined from Kubelka–Munk theory for pure ZnO before and after 50 passages of PLML and for 30 wt% Au NPs on ZnO before and after 50 passages of PLML.

SMS and for ZnO SMS with included Au NPs. An increase of UV extinction for pure ZnO is also observed during PLFL due to the formation of defect-rich ZnO particles.[20] The ZnO SMS obtained after PLML appear yellowish, similar to defect-rich, bandgap-shifted ZnO particles derived from PLFL of ZnO.[20] Thus we attribute the increased UV extinction to the formation of defect-rich ZnO SMS, which is supported by the fluorescence measurements shown in Fig. S6 (ESI†). For the inclusion of Au NPs into ZnO SMS this distinctive increase of UV extinction is not observed. Instead a second extinction peak at around 400 nm to 430 nm occurs. Based on the Kubelka–Munk equations[30,31] we determined the ratio of absorption to scattering K/S from the diffuse reflection spectra, as shown in Fig. 3(d). Absorption caused by the plasmon resonance of Au NPs at around 540 nm can be observed for the educt particles as well as for the Au NP inclusions in ZnO SMS. The plasmon peak of the Au/ZnO educt is broader and less distinctive due to the smaller Au NPs on the surface of the ZnO (see Fig. S7 and S8, ESI,† 0 passages). After 50 passages of PLML this Au NP peak is more distinctive due to the size increase of the gold nanoparticles. From the diagram in Fig. 3(d) we determined the bandgap of the different educts and products. Diagrams and linear fits for the determination of band gap energy, based on the Kubelka–Munk equation and absolute values of diffuse reflection spectra are shown in Fig. S9 in ESI.† Determination of the bandgap energy shows that for both pure ZnO before and after 50 passages of PLML as well as for untreated 30 wt% Au NPs on ZnO the bandgap energy is around 3.23 eV (~384 nm). When Au NPs are included into the ZnO matrix this value decreases to around 3.07 eV (~404 nm). This is in agreement with Chanu *et al.* who integrated Au clusters into ZnO.[32] In similar, the preservation of the plasmon resonance for the integrated plasmonic silver nanoparticles into TiO_2 and the related photocatalytic activity was demonstrated by Awazu *et al.*[33] The Au NPs integrated into ZnO SMS also possess plasmonic properties, as shown in Fig. 3(d).

Obviously, during PLML of supported Au NPs on ZnO a significant increase of the Au NP size is observed at an almost constant ZnO volume. Fig. 4(a) shows the particle size distribution of the gold nanoparticles before and after PLML. The size of the Au NPs measured by SEM (see Fig. S4, ESI†) increases after PLML from ~5 nm to ~17 nm, by about a factor of 3. This means that the zinc oxide microparticles and gold nanoparticles have obviously been transferred into a molten state and both resolidify as spheres, with the gold granules inside the ZnO. The evolution of the crystallite size shown in Fig. 4(d) proves that already after 10 passages Au NPs with diameters around 30–40 nm are formed, and do not change significantly during the additional passages. The increase of the Au NPs size causes a shift of surface plasmon resonance wavelength and an increase of intensity. Thus embedding plasmonic particles into semiconductors causes the enhancement of light absorption,

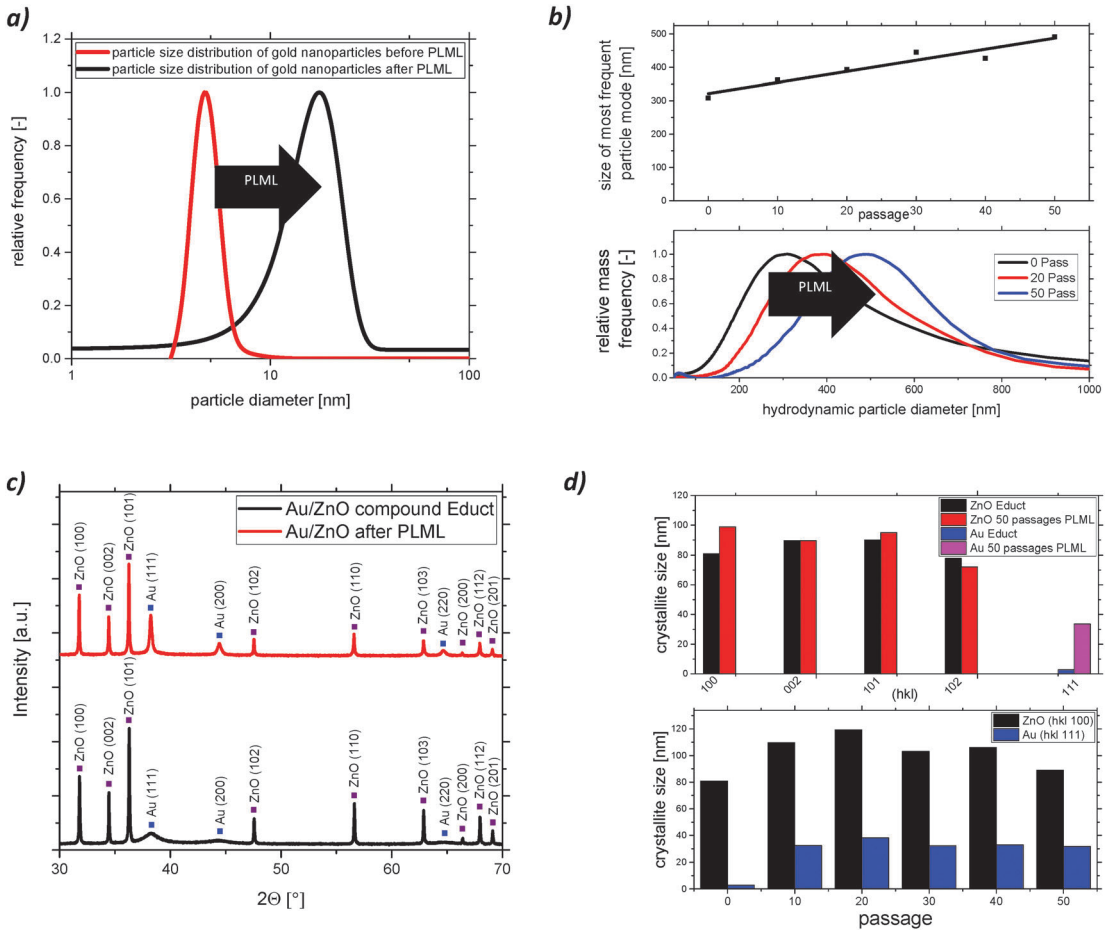

Fig. 4 (a) Particle size distribution of gold nanoparticles before (red curve, supported on zinc oxide) and after (black curve, integrated into zinc oxide sub-micrometer spheres) PLML detected by analytical disc centrifuge measurements (before PLML) and determined by a Gaussian fit from histograms taken from SEM images (after PLML) for 30 wt%; (b) size shift and particle size distribution of the 30 wt% Au NP on ZnO compound after 0, 20 and 50 passages; (c) XRD pattern of the gold zinc oxide compound with 30 wt% Au NP before and after 50 passages exposed to PLML conditions and (d) crystallite size calculated from the XRD pattern and evolution of crystallite size after each 10 passages from 0 to 50 irradiation cycles.

becoming naturally more distinct if the size of the Au NPs is increased, as is known for silver nanoparticles integrated into semiconductors.[34] The XRD pattern reveals the crystallinity of the two materials whereby a size increase of the gold nanoparticles is confirmed (Fig. 4(c) and (d)). The SEM images in Fig. 5(c) and (d) validate the fabrication of sub-micrometer spheres for zinc oxide with 5 wt% Au NPs and 30 wt% Au NPs at a laser fluence of $\sim$80 mJ cm^{-2} at the liquid jets' surface. This is in agreement with Tsuji *et al.* who observed similar SMS particle sizes after PLML at 100 mJ cm^{-2}.[12] At laser fluences of 380 mJ cm^{-2} or higher no PLML can be observed (see Fig. 2(a) and Fig. S3, ESI†), but a reduction in hydrodynamic particle diameter occurs (starting at laser fluences above $\sim$200 mJ cm^{-2}), confirmed by the ADC analysis of hydrodynamic particle diameter shown in Fig. S5 (ESI†). For lower laser fluences no or only slight increase in particle size is obtained, indicating an almost isochoric particle melting (of primary particles and aggregates) and resolidification, similar to the findings on particle reshaping by Nakamura *et al.* and Liu *et al.*[13,23]

The integration of the Au NP into the volume of its ZnO support was determined by correlated SEM images taken with both a secondary electron detector and a back scattered electron detector (Fig. 5(c) and (d)).

The former is more sensitive to the surface topography (lower penetration depth of electrons) and the latter is more sensitive to elemental contrast (higher penetration depth), thus depicting Au NPs in higher contrast to zinc oxide.

Additional SEM images are shown in Fig. S7 and S8 (ESI†). A quantitative transformation of surface-adsorbed gold into inclusions inside zinc oxide sub-micrometer spheres is obtained after 50 passages of laser irradiation with 80 mJ cm^{-2}. SEM images showing the evolution of the Au NP inclusion into ZnO SMS after each 10 passages are depicted in Fig. S10 (ESI†).

Regarding the control of the educt mass flow, Fig. 5(a) illustrates the process of PLML in a sequential liquid flow with defined volume flow rates. The liquid jet is formed by a capillary and the laser is focused perpendicular on the liquid. Particles passing the irradiated volume are transferred into the molten state. Fig. 5(d) shows that different sizes of included Au NPs can be obtained. Due to the cumulation of irradiation cycles (passages) it might be possible that previously formed

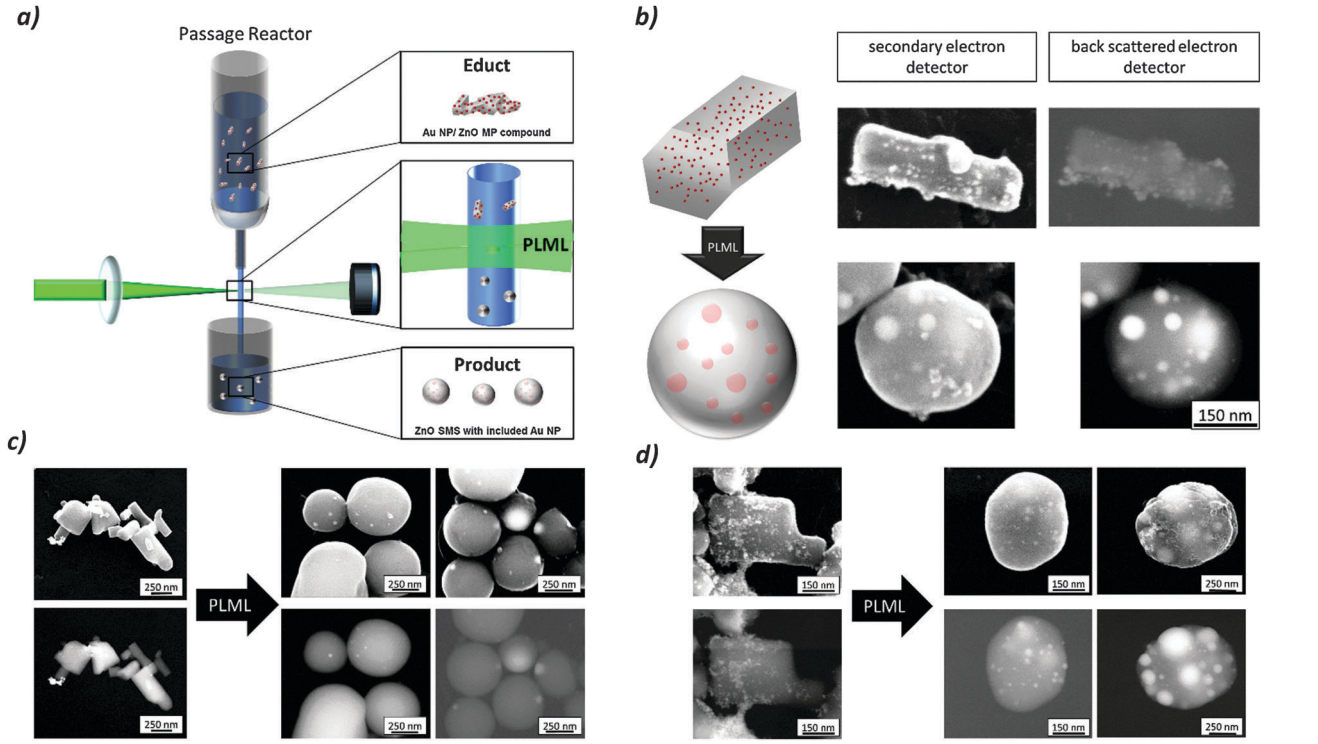

Fig. 5 (a) Illustration of the set-up for laser irradiation of particles in a free liquid flow, changing the particles' morphology from educt to product downstream during PLML; (b) schematic illustration of the Au NP/ZnO MP compound before PLML with nanoparticles adsorbed onto the support and after PLML with the inclusion of nanoparticles (left) and SEM images of the corresponding particles (right); (c) zinc oxide particles with 5 wt% of gold nanoparticles before (left) and after (right) PLML (50 passages) imaged with a secondary electron detector (top row) and a back scattered electron detector (bottom row); (d) zinc oxide particles with 30 wt% of gold nanoparticles before (left) and after (right) PLML (50 passages) imaged with a secondary electron detector (top row) and a back scattered electron detector (bottom row).

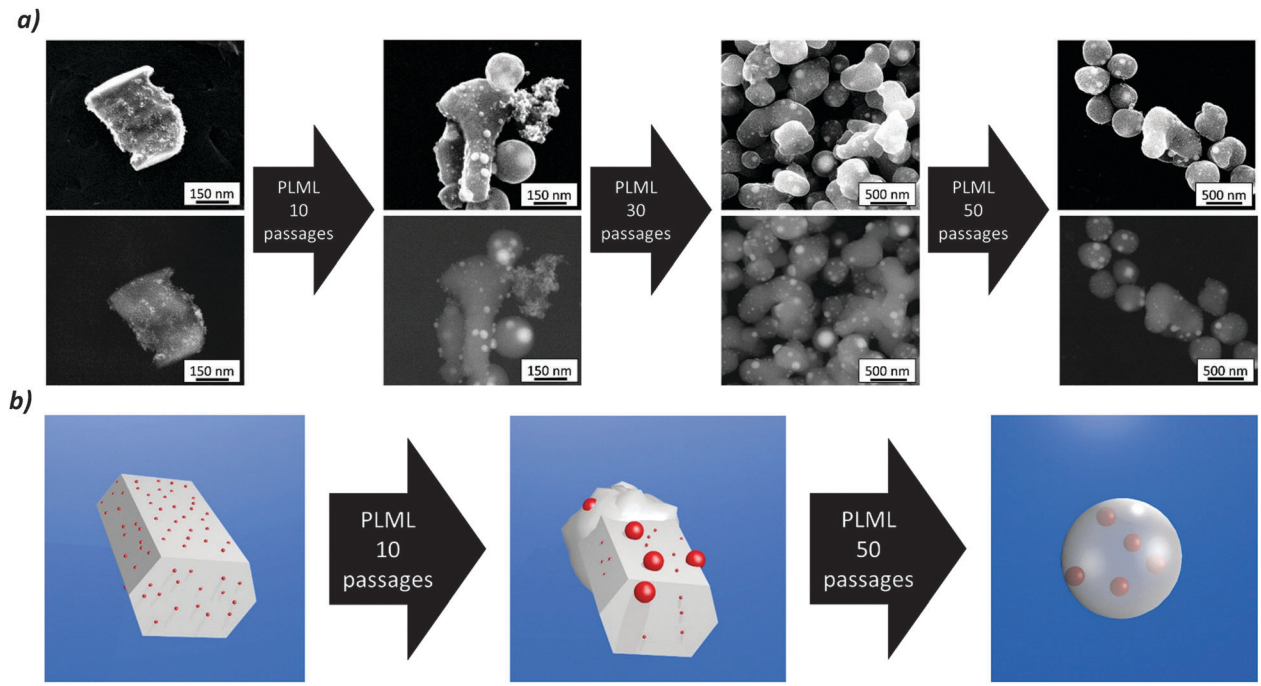

Fig. 6 Evolution of crystalline Au NP inclusion into the ZnO support for a different number of irradiation passages; (a) SEM images of educt (left) and after 10, 30 and 50 passages of PLML detected with a secondary electron detector (top images) and a back scattered electron detector (bottom images) showing evolution of Au (bright) and ZnO particle morphology, and (b) schematic illustration of the evolution from the adsorbed Au NPs on ZnO (educt) *via* intermediate state with size-increased Au NPs (see XRD in Fig. 4) on reshaped ZnO towards included Au NPs in the spherical ZnO matrix (product).

SMS are remolten thus giving the possibility of Au NPs fusing to larger NPs. Fig. 5(b) sketches the transformation from supported Au NP on ZnO towards Au NP inclusions within ZnO SMS by PLML, with corresponding SEM images. SEM images before PLML and after 10, 30 and 50 passages, shown in Fig. 6(a), demonstrate that the Au NP size increases already after 10 passages and that they are not completely included into the ZnO matrix in the intermediate state of the processing. This formation of crystalline Au NPs is in agreement with the sizes determined by the XRD peak analysis, shown in Fig. 4(d). The Scherrer equation reveals that crystalline Au NPs with a diameter of around 30 nm form already after 10 passages and do not change their size significantly afterwards. The SEM images after 10 passages (Fig. 6(a)) demonstrate the different appearance of non-included and included Au NPs. After 30 and 50 passages no more Au NPs adsorbed on the ZnO particles' surface are observed, but their inclusion into the ZnO spheres is obvious. A mechanistic hypothesis of the process evolution is illustrated in Fig. 6(b).

From the UV-vis spectra it can be concluded that the generated Au/ZnO hybrid SMS feature interesting optical properties with two local extinction peaks, as known for gold nanorods, but with completely spherical particles.

Conclusions

In summary, the integration of metals, in particular plasmonic nanoparticles into a submicron-confined semiconductor (or dielectric) volume is challenging, but could provide unique structural and optical properties. Here it is shown that pulsed laser melting of supported gold/zinc oxide particles enables the embedding of plasmonic nanoparticles into a semiconductor matrix isochorically forming monomodal sub-micrometer spheres. The use of monodisperse and ligand-free gold nanoparticles allowed high nanoparticle loads onto the zinc oxide surface and to investigate its structural inversion. During processing, the gold nanoparticles first increase in size and are subsequently transferred during additional irradiation passages into their spherical support. The investigation of the structural morphology and the elemental contrast of the particles by correlated electron microscopy confirmed the integration of the metal nanoparticles into the semiconductor solid spheres. The liquid flow passage reactor allows the characterization of the material properties after each passage with a defined laser energy dose,[20] providing sequential ''snapshots'' of the evolution of the process, and mechanistic insight into the pulsed laser melting of supported particles. Hence nanoparticulate surface adsorbates, widely available as raw materials for catalysis, have been integrated as a solid inclusion into their support.

Acknowledgements

We thank Bernardo Oliviera de Viestel for experimental support during the PLML of the gold/zinc oxide hybrid particles.

References

1 M. Stratakis and H. Garcia, *Chem. Rev.*, 2012, **112**, 4469–4506.
2 W. Yu, M. D. Porosoff and J. G. Chen, *Chem. Rev.*, 2012, **112**, 5780–5817.
3 J. C. Meier, C. Galeano, I. Katsounaros, J. Witte, H. J. Bongard, A. A. Topalov, C. Baldizzone, S. Mezavilla, F. Schüth and K. J. J. Mayrhofer, *Beilstein J. Nanotechnol.*, 2014, **5**, 44–67.
4 J. Strunk, K. Kaehler, X. Xia, M. Comotti, F. Schueth, T. Reinecke and M. Muhler, *Appl. Catal., A*, 2009, **359**, 121–128.
5 P. Li, Z. Wei, T. Wu, Q. Peng and Y. Li, *J. Am. Chem. Soc.*, 2011, **133**, 5660–5663.
6 M. Lau, R. G. Niemann, M. Bartsch, W. O'Neill and S. Barcikowski, *Appl. Phys. A: Mater. Sci. Process.*, 2014, **114**, 1023–1030.
7 Y. Ishikawa, Y. Shimizu, T. Sasaki and N. Koshizaki, *Appl. Phys. Lett.*, 2007, **91**, 161110.
8 H. Wang, N. Koshizaki, L. Li, L. Jia, K. Kawaguchi, X. Li, A. Pyatenko, Z. Swiatkowska-Warkocka, Y. Bando and D. Goldberg, *Adv. Mater.*, 2011, **23**, 1865–1870.
9 X. Hu, H. Gong, Y. Wang, Q. Chen, J. Zhang, S. Zheng, S. Yang and B. Cao, *J. Mater. Chem.*, 2012, **22**, 15947–15952.
10 H. Fujiwara, R. Niyuki, Y. Ishikawa, N. Koshizaki, T. Tsuji and K. Sasaki, *Appl. Phys. Lett.*, 2013, **102**, 061110.
11 H. Wang, K. Kawaguchi, A. Pyatenko, X. Ki, Z. Swiatkowska-Warkocka, Y. Katou and N. Koshizaki, *Chem. – Eur. J.*, 2012, **18**, 163–169.
12 T. Tsuji, Y. Higashi, M. Tsuji, H. Fujiwara, Y. Ishikawa and N. Koshizaki, *J. Laser Micro/Nanoeng.*, 2013, **8**, 292–295.
13 D. Liu, C. Li, F. Zhou, H. Zhang, X. Li, G. Duan, W. Cai and Y. Li, *Sci. Rep.*, 2014, **5**, 7686.
14 S. Link and M. A. El-Sayed, *J. Phys. Chem. B*, 1999, **103**, 8410–8426.
15 S. Link and M. A. El-Sayed, *J. Phys. Chem. B*, 1999, **103**, 4212–4217.
16 S. Link, C. Burda, M. B. Mohamed, B. Nikoobakht and M. A. El-Sayed, *J. Phys. Chem. A*, 1999, **103**, 1165–1170.
17 S. Inasawa, M. Sugiyama and Y. Yamaguchi, *J. Phys. Chem. B*, 2005, **109**, 3104–3111.
18 T. Tsuji, T. Yahata, M. Yasutomo, K. Igawa, M. Tsuji, Y. Ishikawa and N. Koshizaki, *Phys. Chem. Chem. Phys.*, 2013, **15**, 3099–3107.
19 T. Tsuji, Y. Higashi, M. Tsuji, Y. Ishikawa and N. Koshizaki, *Appl. Surf. Sci.*, 2015, **348**, 10–15.
20 M. Lau and S. Barcikowski, *Appl. Surf. Sci.*, 2015, **348**, 22–29.
21 Y. Ishikawa, Q. Feng and N. Koshizaki, *Appl. Phys. A: Mater. Sci. Process.*, 2010, **99**, 797–803.
22 Z. Swiatkowska-Warkocka, K. Koga, K. Kawaguchi, H. Wang, A. Pyatenko and N. Koshizaki, *RSC Adv.*, 2013, **3**, 79–83.
23 M. Nakamura, A. Oyane, I. Sakamaki, Y. Ishikawa, Y. Shimizu and K. Kawaguchi, *Phys. Chem. Chem. Phys.*, 2015, **17**, 8836–8842.
24 K. Kawaguchi, J. Jaworski, Y. Ishikawa, T. Sasaki and N. Koshizaki, *IEEE Trans. Magn.*, 2006, **42**, 3620–3622.
25 K. Kawaguchi, J. Jaworski, Y. Ishikawa, T. Sasaki and N. Koshizaki, *J. Magn. Magn. Mater.*, 2007, **310**, 2369–2371.

26 Z. Swiatkowska-Warkocka, K. Kawaguchi, Y. Shimizu, A. Pyatenko, H. Wang and N. Koshizaki, *Langmuir*, 2012, **28**, 4903–4907.
27 P. Wagener, A. Schwenke and S. Barcikowski, *Langmuir*, 2012, **28**, 6132–6140.
28 G. Marzun, J. Nakamura, X. Zhang, S. Barcikowski and P. Wagener, *Appl. Surf. Sci.*, 2015, **348**, 75–84.
29 P. Stamatakis, B. R. Palmer, G. C. Salzmanm, C. F. Bohren and T. B. Allen, *J. Coat. Technol.*, 1990, **62**, 95–98.
30 P. Kubelka and F. Munk, *Z. Tech. Phys.*, 1931, **12**, 593–601.
31 P. Kubelka, *J. Opt. Soc. Am.*, 1948, **38**, 448–457.
32 T. I. Chanu, T. Muthukumar and P. T. Manoharan, *Phys. Chem. Chem. Phys.*, 2014, **16**, 23686–23698.
33 K. Awazu, M. Fujimaki, C. Rockstuhl, J. Tominaga, H. Murakami, Y. Ohki, N. Yoshida and T. Watanabe, *J. Am. Chem. Soc.*, 2008, **130**, 1676–1680.
34 P. Spinelli and A. Polman, *Opt. Express*, 2012, **20**, A641–A654.

